Magnetic Field Prediction in Cubic Spoke-Type Permanent-Magnet Machine Considering Magnetic Saturation

Du, Yunlu; Huang, Yunkai; Guo, Baocheng; Djelloul-Khedda, Zakarya; Peng, Fei; Yao, Yu; Dong, Jianning

DOI
10.1109/TIE.2023.3265043

Publication date
2024

Document Version
Final published version

Published in
IEEE Transactions on Industrial Electronics

Citation (APA)
Du, Y., Huang, Y., Guo, B., Djelloul-Khedda, Z., Peng, F., Yao, Y., & Dong, J. (2024). Magnetic Field Prediction in Cubic Spoke-Type Permanent-Magnet Machine Considering Magnetic Saturation. *IEEE Transactions on Industrial Electronics*, *71*(3), 2208-2219. https://doi.org/10.1109/TIE.2023.3265043

Magnetic Field Prediction in Cubic Spoke-Type Permanent-Magnet Machine Considering Magnetic Saturation

Yunlu Du, *Student Member, IEEE*, Yunkai Huang, Baocheng Guo, *Member, IEEE*,
Zakarya Djelloul-Khedda, Fei Peng, *Member, IEEE*, Yu Yao, *Student Member, IEEE*,
and Jianning Dong, *Member, IEEE*

***Abstract*—In this article, a nonlinear semianalytical model (SAM) is presented to predict the magnetic field distribution (MFD) and electromagnetic performances (EPs) in the cubic spoke-type permanent magnet (PM) machine. To model the rectangular PMs, the rectangular PM is simplified as a combination of fan-shaped regions with different arc angles. Then, the MFD and EPs of the cubic spoke-type machines can be obtained by the harmonic modeling technique. Particularly, the saturation of the magnetic bridges is considered by the nonlinear iterative algorithm. The proposed nonlinear SAM is studied on a 12-slot/8-pole cubic PM prototype, and the nonlinear finite element model and experiment verify its correctness. The main contribution of this article is to present a general analytical modeling method for cubic spoke-type PM machines and consider the magnetic saturation of magnetic bridges.**

***Index Terms*—Cubic spoke-type permanent magnet (PM) machine, harmonic modeling (HM), magnetic saturation, nonlinear.**

NOMENCLATURE

PM	Permanent magnet.
FE model	Finite-element model.
SD	Subdomain.
HM	Harmonic modeling.
SAM	Semianalytical model.
MFD	Magnetic field distribution.
CFS	Complex Fourier series.
A	Magnetic vector potential.
B	Magnetic flux density.
H	Magnetic field strength.
μ	Permeability.
M	Magnetization.
J	Current density.

I. INTRODUCTION

As a typical topology of the interior permanent magnet (PM) machine, the tangentially magnetized spoke-type PM machine has a good flux concentrated effect, compared with other types of PM machines, which provides better performance [1], [2], [3]. Therefore, spoke-type PM machines have extensive application prospects in industrial and household appliances [4], [5]. It is crucial to develop a rapid and precise magnetic field distribution (MFD) calculation approach for its design and optimization.

Finite element (FE) analysis has obvious advantages in precisely predicting the magnetic field of complex structure motors as it can take into account the influence of nonlinear ferromagnetic material [6], [7], [8]. Nevertheless, the optimization of the spoke-type PM machine necessitates numerous geometrical dimension iterations, which takes a lot of time [9]. The alternative strategy is analytical or hybrid analysis, which can rapidly evaluate the motor's magnetic field [10]. Numerous analytical models have been developed over the years [11], [12], [13], [14]. However, most of the analytical models cannot consider the nonlinear effect of iron parts, that is, the saturation is ignored, which leads to the overestimation of the magnetic field [15]. To take the effect of the magnetic saturation into consideration, Dubas and Boughra proposed an exact SD model that considers material nonlinearity by superimposing the components of the magnetic field solution in each subdomain of r- and θ-directions (or x- and y-directions) [16], [17]. Besides, the local saturation effect can be further considered by dividing the iron part into elementary subdomains [18]. The harmonic modeling (HM) approach presented in [19] and [20] directly embeds the permeability of ferromagnetic materials into the magnetostatic field solution, in contrast to the analytical models developed in [16] and [17]. HM technology is further developed by DjelloulKhedda et al., which is used to compute the performances of

Manuscript received 29 September 2022; revised 10 January 2023 and 26 February 2023; accepted 25 March 2023. Date of publication 11 April 2023; date of current version 14 September 2023. This work was supported in part by the National Natural Science Foundation of China under Grant 52277036. *(Corresponding author: Fei Peng.)*

Yunlu Du, Yunkai Huang, Fei Peng, and Yu Yao are with the School of Electrical and Automation Engineering, Southeast University, Nanjing 210023, China (e-mail: duyl@seu.edu.cn; huangyk@seu.edu.cn; pengfei@seu.edu.cn; yuyao@seu.edu.cn).

Baocheng Guo is with the School of Electrical and Automation Engineering, Nanjing Normal University, Nanjing 210023, China (e-mail: bc.guo@njnu.edu.cn).

Zakarya Djelloul-Khedda is with the Electrotechnique, Universite de Khemis Miliana, Khemis Miliana 44225, Algeria (e-mail: djelloulkhedda.zakarya@chlef.sng-dist.dz).

Jianning Dong is with the Department of Electrical Sustainable Energy, Delft University of Technology, 2628DC Delft, The Netherlands (e-mail: j.dong-4@tudelft.nl).

Color versions of one or more figures in this article are available at https://doi.org/10.1109/TIE.2023.3265043.

Digital Object Identifier 10.1109/TIE.2023.3265043

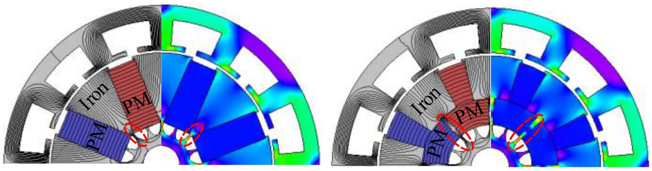

(a) (b)

Fig. 1. Equivalent calculation method of a spoke-type PM machine. (a) Initial model. (b) Equivalent model.

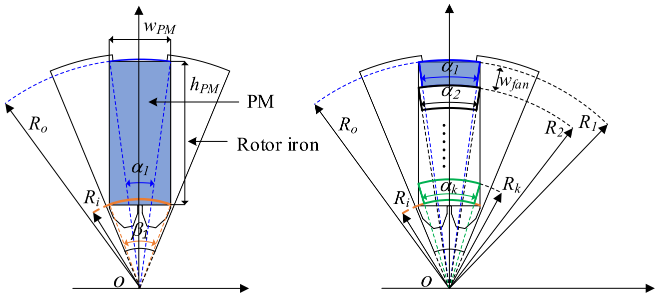

(a) (b)

Fig. 2. Improved modeling method of rectangular PM. (a) Initial rectangular PM. (b) Equivalent fan-shaped region.

the switched reluctance machine [21] and the iron-core loss of the flux-modulated PM machine [22]. Based on HM technology, Zhao et al. proposed a rapid optimization technique for coaxial magnetic gears that takes only around 80% as long to compute as the FE model takes [23]. Therefore, the nonlinear semianalytical model (SAM) based on HM technology is an effective approach to design and optimize the spoke-type PM machine.

The analytical modeling of spoke-type PM machines with regular forms in polar coordinates has attracted some academic attention, and it is relatively straightforward [13], [24], [25]. On the other hand, it is challenging to approximate cube spoke-type PMs as subdomains that are consistent in polar coordinates. To solve this problem, Meessen et al. [26] provided a reference solution for transforming an inconsistent domain into the consistent domain of the reference coordinate. On this basis, the rectangular PMs can be approximated by several fan-shaped subdomains [27], [28], [29], [30]. The rectangular PM is equivalent to two fan-shaped regions by Liang et al., and the exact SD model (the nonlinearity of ferromagnetic materials is ignored) is used to determine the MFD and electromagnetic performances of a spoke-type PM machine. However, as the majority of spoke-type PMs are designed with long depths and wide widths, it is not a generally accepted modeling technique to roughly transform a rectangular PM into two fan-shaped sections [28], [29], [30]. The MFD of the initial model and equivalent model of a spoke-type PM motor is evaluated using the FE model, as illustrated in Fig. 1, in accordance with the authors provided in [28], [29], and [30]. It is clear that the spoke-type PM motor's unique structure causes the magnetic flux leakage of the equivalent model to increase and the saturation of the rotor core to intensify. As a result, this method cannot be used to model the spoke-type PM motor analytically in general. On the other hand, because the traditional SD model disregards magnetic saturation, the magnetic flux density will be exaggerated. For analytical modeling, it is essential to determine the geometric parameters of each approximated fan-shaped region (such as the inner/outer radius, polar-arc angle, etc.) [27]. Therefore, it is necessary to propose a general modeling method for cubic spoke-type PM motors to quickly and accurately calculate their MFD and electromagnetic performances (EPs).

This article proposes an improved SAM for magnetic field prediction in cubic spoke-type PM motors based on HM technology to solve the aforementioned issues. The influence of local saturation of the magnetic bridge can be accurately taken into consideration by an iterative algorithm. The FE model and experiments are utilized to verify the validity of the proposed nonlinear SAM. The approach described in this article is applicable to all cubic spoke-type PM machines, has significant theoretical significance, and serves as an engineering reference for the design and optimization of such machines.

The rest of this article is organized as follows. The improved rectangular PM modeling approach and model simplification are introduced in Section II. Section III presents the spoke-type PM SAM in polar coordinates. In Section IV, the results of the proposed SAM are compared with those of the FE model. The prototype is then tested in Section V. Finally, Section VI concludes this article.

II. MODEL SIMPLIFICATION

This section introduces the improved modeling approach for rectangular PM and simplifies the rotor and stator.

A. Model of Rectangular PM

In polar coordinates, to satisfy partial differential equations and boundary conditions, the geometry of PM should be a regular region [27]. As a result, as shown in Fig. 2, the rectangular PM in this article is approximated by a superposition of fan-shaped regions with different pole-arc angles. The geometric parameters of each fan-shaped region can be determined by mathematical formulas as follows.

The width of each fan-shaped region w_{fan} is

$$w_{\text{fan}} = \frac{R_o - R_i}{K} \tag{1}$$

where K is the number of fan-shaped regions; R_o and R_i are the inner and outer radii of the rectangular PM, respectively.

The outer radius of the first fan-shaped region is R_1 ($R_1 = R_o$), and the kth outer radius is

$$R_o^k = R_1 - W_{\text{fan}}\left(k - 1\right). \tag{2}$$

Then, the polar-arc angle corresponding to each fan-shaped region can be calculated by

$$\alpha_k = 2 \cdot \arcsin\left(\frac{W_{PM}}{2 \cdot R_o^k}\right). \tag{3}$$

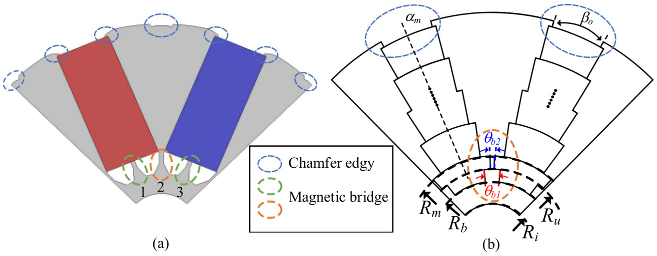

Fig. 3. Structure of the rotor. (a) Initial structure. (b) Simplified structure.

The inner radius can be obtained by

$$R_i^k = \alpha_k \cdot (R_1 - k \cdot W_{\text{fan}}) . \tag{4}$$

The area $S^k{}_f$ of each fan-shaped region is

$$S_f^k = \left[\left(R_o^k\right)^2 - \left(R_i^k\right)^2 \right] \cdot \alpha_k . \tag{5}$$

To maintain the same magnetic energy [28], it is necessary to introduce the area coefficient f_s to compensate for the change in magnetic energy (the effective length L_{ef} remains constant). The magnetic energy W_c of cubic PM and W_f of fan-shaped PMs are respectively [31]:

$$W_c = \frac{S_c L_{ef} B_{r,c}^2}{2\mu_r \mu_0} \tag{6}$$

$$W_f = \frac{\sum_{k=1}^{K} S_f^k L_{ef} B_{r,f}^2}{2\mu_r \mu_0} \tag{7}$$

where S_c and S_f, $B_{r,c}$ and $B_{r,f}$ are the area and remanence density of cubic PM and fan-shaped PMs, respectively.

Then, the equivalent remanence density $B_{r,f}$ of the fan-shaped PMs can be obtained as

$$B_{r,f} = (f_s)^{1/2} \cdot B_{r,c} \tag{8}$$

$$f_s = \frac{S_c}{S_f} = \frac{w_{PM} \cdot h_{PM}}{\sum_{k=1}^{K} S_f^k} . \tag{9}$$

It should be noted that this is a general rectangular PM modeling method, and each fan-shaped region of the inner/outer radius, polar-arc angle, and other geometric parameters are accurately defined.

B. Simplification of Rotor and Stator Structure

TABLE I
SIMPLIFIED DIMENSIONS OF ROTOR STRUCTURE

Items	Symbol	Value
Outer radius of rotor	R_r	41.65 mm
Radius of outer PM	R_o	40.57 mm
Radius of inner PM	R_i/R_m	15.68 mm
The radius of the top magnetic bridge	R_u	13.27 mm
The radius of the bottom magnetic bridge	R_b	11 mm
Rotor slots width angle	β_o	13.58°
Top magnetic bridges width angle	θ_{b2}	2.92°
Bottom magnetic bridges width angle	θ_{b1}	13°

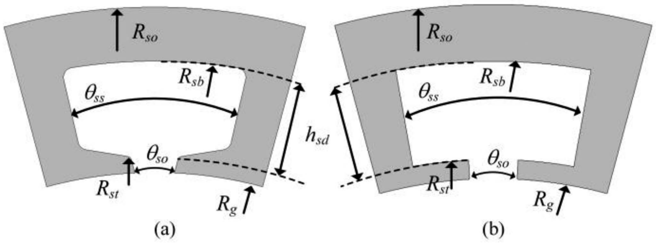

Fig. 4. Structure of the stator. (a) Initial structure. (b) Simplified structure.

TABLE II
SIMPLIFIED DIMENSIONS OF STATOR STRUCTURE

Items	Symbol	Value
Radius of slot bottom	R_{sb}	54 mm
Radius of slot top	R_{st}	44.5 mm
Radius of inner stator	R_g	42.65 mm
Slot width angle	θ_{ss}	20.22 °
Slot opening angle	θ_{so}	6.18°

The permeability distribution of rotor iron becomes uneven as a result of the leakage fluxes passing through the magnetic bridges, which causes saturation [10]. The top of the magnetic bridge is thin and the bottom is thick to limit the leakage flux and guarantee mechanical strength, as shown in Fig. 3(a). The leakage fluxes almost do not pass the magnetic bridge “1” and “3,” they only play a mechanical supporting role. Therefore, they are ignored in the analytical model. Then, magnetic bridge “2” is equivalent to two fan-shaped magnetic bridges, and the arc angles are θ_{b1} and θ_{b2}, respectively. Additionally, the rotor chamfer at the rotor slot opening is simplified as a fan-shaped area, and the chamfer at the rotor top is ignored. The simplified rotor structure and parameters are shown in Fig. 3(b) and Table I, respectively.

The saturation effect of the magnetic bridge in the rotor core is the most obvious. The saturation effect can be considered more accurately by dividing iron parts along with radial and tangential directions, which will be introduced in the following section.

In addition, the stator slot in the analytical model is simplified to an equal angle width, while the stator slot-opening angle and radius remain unchanged. The simplified stator structure and parameters are shown in Fig. 4 and Table II, respectively.

III. SEMIANALYTICAL MODEL

The 2-D analytical model can be easily obtained through the aforementioned simplifications and is divided into the following straightforward categories. As illustrated in Fig. 5, S_I represents the stator slots/teeth, S_{II} is the stator tooth tip, S_{III} is the air gap, $S^R{}_I$ represents rotor slots opening, $S^P{}_I \sim S^P{}_k$ represent PMs, $S^B{}_I$ and $S^B{}_{II}$ are magnetic bridges. The partial differential equation satisfied by each region can be derived by introducing the magnetic vector potential.

A. Stator Slots/Teeth Region

The angular position of the i_{th} stator slot opening is defined by

$$\begin{cases} \alpha_i = \frac{2\pi}{Q_s} i - \frac{\pi}{Q_s} \\ i = 1, 2, \cdots, Q_s . \end{cases} \tag{10}$$

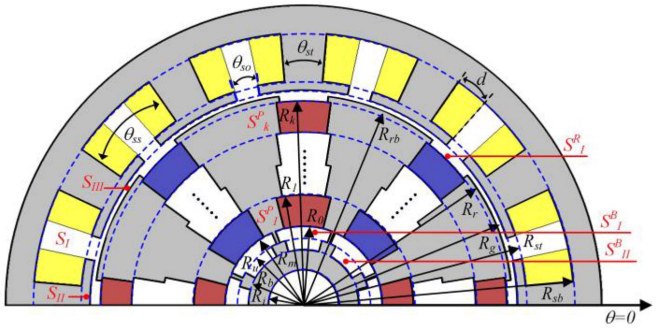

Fig. 5. 2-D analytical model.

The magnetic vector potential A_{SI} satisfies the following Poisson equation [21]:

$$\frac{\partial^2 A_z^{S_I}}{\partial r^2}+\frac{1}{r}\frac{\partial A_z^{S_I}}{\partial r}-\left(\frac{V_{S_I}}{r}\right)^2 A_z^{S_I}=-\mu_{c,\theta}^{S_I}J_z \tag{11}$$

where $V_{S_I}=\left[\mu_{c,\theta}^{S_I}K_\theta(\mu_{c,r}^{S_I})^{-1}K_\theta\right]^{1/2}$.

The general solution of (11) is

$$A_z^{S_I}\big|_r=W_{S_I}\left(\frac{r}{R_{sb}}\right)^{\lambda_{S_I}}a_{S_I}+W_{S_I}\left(\frac{R_s}{r}\right)^{\lambda_{S_I}}b_{S_I}+r^2F \tag{12}$$

where a_{S_I} and b_{S_I} are unknown coefficients.

The particular solution of (11) is r^2F, and F is defined by

$$F=\left([V_{S_I}]^2-4I\right)^{-1}\mu_{c,\theta}J_z \tag{13}$$

where J_z is the complex Fourier series (CFS) coefficients of J, which can be obtained by

$$\begin{aligned}\hat{J}_{z,n}=\frac{1}{2\pi jn}\sum_{i=1}^{Q_s}\Big[&J_{i,1}\left(e^{jnd}-1\right)e^{-jn\frac{\theta_{ss}}{2}}\\&+J_{i,2}\left(1-e^{-jnd}\right)e^{jn\frac{\theta_{ss}}{2}}\Big]e^{jn\alpha_i}\end{aligned} \tag{14}$$

$$J_{i,1}=\frac{N_c}{S}C_1^T\left[i_A,i_B,i_C\right] \tag{15}$$

$$J_{i,2}=\frac{N_c}{S}C_2^T\left[i_A,i_B,i_C\right] \tag{16}$$

where N_c is the conductor number of slot coil, $[i_A, i_B, i_C]$ are the armature currents, S is the surface of the stator slot coil, $C_1{}^T$ and $C_2{}^T$ are the transpose of the connecting matrix between the three-phase current and the stator slots, which represent the distribution of stator windings in the slots

$$J_z=\left[\hat{J}_{z,-N}\quad\cdots\quad\hat{J}_{z,N}\right]^T. \tag{17}$$

B. PM Region

The magnetic vector potential in the PM region satisfies the following Poisson's equation [23]:

$$\begin{aligned}&\frac{\partial^2 A_z^{S_{Pk}}}{\partial r^2}+\frac{1}{r}\frac{\partial A_z^{S_{Pk}}}{\partial r}-\left(\frac{V_{S_{Pk}}}{r}\right)^2 A_z^{S_{Pk}}\\&=-\frac{\mu_0}{r}\left(M_\theta^k+jK_\theta M_r^k\right)\end{aligned} \tag{18}$$

where $M_r{}^k$ and $M_\theta{}^k$ are the CFS coefficients of radial and tangential components of the magnetization vector M

$$\hat{M}_{\theta,n}^k=\frac{2pB_{r,f}}{n\pi\mu_0}\sin\left(\frac{n\pi}{2p}\alpha_k\right) \tag{19}$$

$$\hat{M}_{r,n}^k=0 \tag{20}$$

$$M_\theta^k=\left[\hat{M}_{r,-N}^k\quad\cdots\quad\hat{M}_{r,N}^k\right]^T. \tag{21}$$

The general solution of (18) is

$$A_z^{P_k}\big|_r=W_{P_k}\left(\frac{r}{R_k}\right)^{\lambda_{S_I}}a_{P_k}+W_{P_k}\left(\frac{R_{k-1}}{r}\right)^{\lambda_{P_k}}b_{P_k}+rG. \tag{22}$$

The particular solution of (18) is rG , and G is defined by

$$G=\mu_0\left(V_{P_k}^2-I\right)^{-1}\left(M_\theta^k+jK_\theta M_r^k\right). \tag{23}$$

C. Other Regions

The magnetic vector potential in the stator slot-opening region, air-gap region, rotor-slot opening region, and magnetic bridge region satisfies the following Laplace equation [20]:

$$\frac{\partial^2 A_z^{S_m}}{\partial r^2}+\frac{1}{r}\frac{\partial A_z^{S_m}}{\partial r}-\left(\frac{V_{S_m}}{r}\right)^2 A_z^{S_m}=0. \tag{24}$$

The general solution of (24) is as follows, using the stator slot-opening region as an example

$$A_z^{S_{II}}\big|_r=W_{S_{II}}\left(\frac{r}{R_{st}}\right)^{\lambda_{S_{II}}}a_{S_{II}}+W_{S_{II}}\left(\frac{R_g}{r}\right)^{\lambda_{S_{II}}}b_{S_{II}}. \tag{25}$$

In the air-gap region, $\lambda_{S_{III}}=\sqrt{[K_\theta]^2}=|K_\theta|$.

D. Boundary Conditions

The interface continuity boundary conditions and Newman boundary conditions are collected in Table III based on the overall solutions of the aforementioned subdomains.

Finally, all boundary conditions are written in the following matrix form:

$$MX=Y \tag{26}$$

where M, X, and Y represent the coefficient factors, the unknown coefficients, and the constant values in the boundary condition equations, respectively.

Then, the EPs (including cogging torque, back EMF, electromagnetic torque, etc.) can be further predicted [24]. The calculating formula is as follows:

The electromagnetic torque T_{em} can be computed by

$$T_{em}=\frac{L_{lef}R_g^2}{\mu_0}\int_0^{2\pi}B_r^{II}\left(R_g,\theta\right)B_\theta^{II}\left(R_g,\theta\right)d\theta. \tag{27}$$

The flux linkage of the ith stator slot coil can be computed by

$$\varphi_{1,i}=L_{lef}\frac{N_c}{S}\int_{\alpha_i-\frac{\theta_{ss}}{2}}^{\alpha_i-\frac{\theta_{ss}}{2}+d}\int_{R_{st}}^{R_{sb}}A_z^{IV}\left(r,\theta\right)dr d\theta \tag{28}$$

$$\varphi_{2,i}=L_{lef}\frac{N_c}{S}\int_{\alpha_i+\frac{\theta_{ss}}{2}-d}^{\alpha_i+\frac{\theta_{ss}}{2}}\int_{R_{st}}^{R_{sb}}A_z^{IV}\left(r,\theta\right)dr d\theta. \tag{29}$$

TABLE III
BOUNDARY CONDITIONS

Description	Expressions
BCs between S_I and S_{II}	$A_z^{S_I}\big\|_{r=R_{st}} - A_z^{S_{II}}\big\|_{r=R_{st}} = 0$ $H_\theta^{S_I}\big\|_{r=R_{st}} - H_\theta^{S_{II}}\big\|_{r=R_{st}} = 0$
BCs between S_{II} and S_{III}	$A_z^{S_{II}}\big\|_{r=R_g} - A_z^{S_{III}}\big\|_{r=R_g} = 0$ $H_\theta^{S_{II}}\big\|_{r=R_g} - H_\theta^{S_{III}}\big\|_{r=R_g} = 0$
BCs between S_{III} and S_I^R	$A_z^{S_{III}}\big\|_{r=R_r} - A_z^{S_I^R}\big\|_{r=R_r} = 0$ $H_\theta^{S_{III}}\big\|_{r=R_r} - H_\theta^{S_I^R}\big\|_{r=R_r} = 0$
BCs between S_I^R and S_k^P	$A_z^{S_I^R}\big\|_{r=R_k} - A_z^{S_k^P}\big\|_{r=R_k} = 0$ $H_\theta^{S_I^R}\big\|_{r=R_k} - H_\theta^{S_k^P}\big\|_{r=R_k} = 0$
BCs between S_k^P and $S^P{}_{k-1}$	$A_z^{S_k^P}\big\|_{r=R_{k-1}} - A_z^{S_{k-1}^P}\big\|_{r=R_{k-1}} = 0$ $H_\theta^{S_k^P}\big\|_{r=R_{k-1}} - H_\theta^{S_{k-1}^P}\big\|_{r=R_{k-1}} = 0$
BCs between S_I^P and S_I^B	$A_z^{S_I^P}\big\|_{r=R_m} - A_z^{S_I^B}\big\|_{r=R_m} = 0$ $H_\theta^{S_I^P}\big\|_{r=R_m} - H_\theta^{S_I^B}\big\|_{r=R_m} = 0$
BCs between S_I^B and S_{II}^B	$A_z^{S_I^B}\big\|_{r=R_u} - A_z^{S_{II}^B}\big\|_{r=R_u} = 0$ $H_\theta^{S_I^B}\big\|_{r=R_u} - H_\theta^{S_{II}^B}\big\|_{r=R_u} = 0$
BCs at $r=R_{sb}$	$H_\theta^{S_I}\big\|_{r=R_{sb}} = 0$
BCs at $r=R_b$	$H_\theta^{S_{II}^B}\big\|_{r=R_b} = 0$

The total flux linkage for each phase can be obtained.

$$\begin{bmatrix}\Psi_a\\ \Psi_b\\ \Psi_c\end{bmatrix} = \begin{bmatrix}\Psi_{1,a}\\ \Psi_{1,b}\\ \Psi_{1,c}\end{bmatrix} + \begin{bmatrix}\Psi_{2,a}\\ \Psi_{2,b}\\ \Psi_{2,c}\end{bmatrix} \tag{30}$$

where

$$\begin{bmatrix}\Psi_{1,a}\\ \Psi_{1,b}\\ \Psi_{1,c}\end{bmatrix} = C_1\begin{bmatrix}\varphi_{1,1} & \varphi_{1,2} & \cdots & \varphi_{1,Q_s}\end{bmatrix}^T \tag{31}$$

$$\begin{bmatrix}\Psi_{2,a}\\ \Psi_{2,b}\\ \Psi_{2,c}\end{bmatrix} = C_2\begin{bmatrix}\varphi_{2,1} & \varphi_{2,2} & \cdots & \varphi_{2,Q_s}\end{bmatrix}^T. \tag{32}$$

Then, the back EMF for each phase can be derived as

$$\begin{bmatrix}E_a\\ E_b\\ E_c\end{bmatrix} = -\frac{d}{dt}\begin{bmatrix}\Psi_a\\ \Psi_b\\ \Psi_c\end{bmatrix}. \tag{33}$$

For phase A, the machine is fed only by phase A with i_a, and the self- and mutual inductances can be calculated as follows:

$$\begin{bmatrix}L_a\\ M_{ab}\\ M_{ac}\end{bmatrix} = \begin{bmatrix}\Psi_a & \Psi_b & \Psi_c\end{bmatrix}^T \Big/ i_a. \tag{34}$$

E. Nonlinear Solution Algorithm

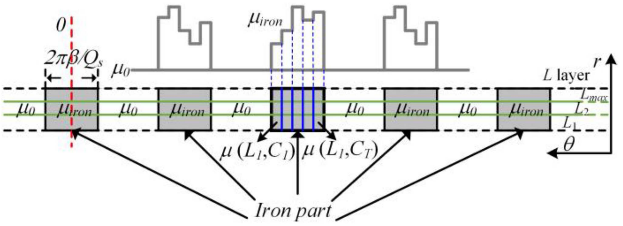

Fig. 6. Multilayer division of iron part.

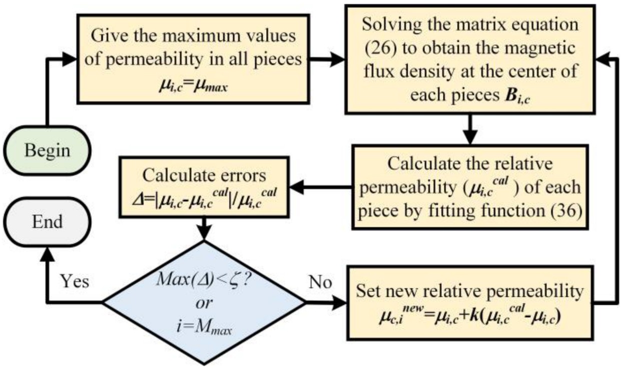

Fig. 7. Nonlinear iterative algorithm.

As illustrated in Fig. 6, each part of the iron can be separated into C_T blocks along the θ-direction and L layers along the r-direction. The Fourier coefficients of the lth layer of the stator slots/teeth region can be obtained by

$$\hat{\mu}_n^l = \begin{cases}(1-\beta)\,\mu_0 + \frac{\beta}{Q_sC_T}\sum_{i=1}^{Q_s}\sum_{c=1}^{C_T}\mu_{i,c} & n=0\\ \sum_{i=1}^{Q_s}\frac{\mu_0}{2\pi jn}e^{jn\pi\frac{2(i-1)-\beta}{Q_s}}\left[1-e^{jn\pi\frac{2(\beta-1)}{Q_s}}\right] & \\ +\sum\limits_{i=1}^{Q_s}\sum\limits_{c=1}^{C_T}\frac{\mu_{i,c}}{2\pi jn}e^{\frac{\beta C_T-2(i-1)C_T-2\beta c}{Q_sC_T}}\left[e^{jn\pi\frac{2\beta}{Q_sC_T}}-1\right] & n\neq 0\end{cases} \tag{35}$$

where $\mu_{i,c}$ is the permeability in the cth piece of the ith iron part.

The Fourier coefficients $\hat{\mu}_n^{l,rec}$ can be obtained by replacing $(\mu_0, \mu_{i,c})$by$(1/\mu_0, 1/\mu_{i,c})$ in (35).

K in Fig. 7 is the correction factor ($0<k<1$), and the empirical value is generally 0.2–0.3 [23]. The algorithm shown in Fig. 7 is utilized to estimate the saturation level in the soft-magnetic material through an iterative process. On the other hand, although the calculation accuracy can be improved by dividing the iron parts into more layers, it sacrifices the calculation time. In the Spoke-type PM motor studied in this article, the magnetic saturation of the rotor magnetic bridge is the most obvious. The effect of magnetic bridge saturation is considered by the iterative algorithm. When the error requirement Δ is met or the maximum number of iterations $M_{\max}$ is reached, the calculation is completed.

The relative permeability can be obtained by the fitting equation [32]

$$\mu_r(B) = \left(\frac{B_o}{H_o\mu_0}\right)\left(\frac{1}{1+(B/B_o)^{v-1}}\right) \tag{36}$$

where B_o, H_o, and v are the constants.

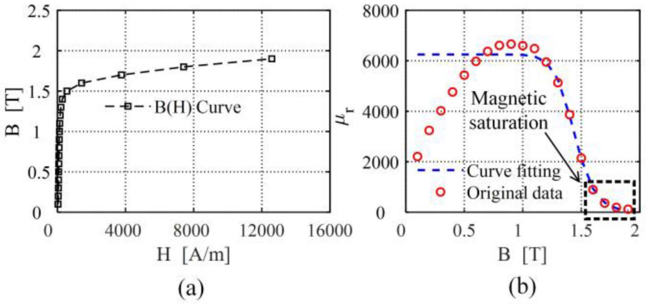

Fig. 8. Magnetic characteristic of 50CS470. (a) *B-H*. (b) μ_r-*B*.

TABLE IV
MAIN PARAMETERS OF THE STUDIED MACHINE

Items	Symbol	Value
Number of slots	Q_s	12
Number of pole pairs	p	4
Rated current	I	10 A
Number of turns	N_c	14
Active length	L_{lef}	14 mm
Remanence of PM	B_r	0.47 T

The ferromagnetic material adopted in this prototype is 50CS470, and its *B-H* curve and *B*-μ_r curve are given in Fig. 8. The parameters B_o, H_o, and v are 1.44, 133.3, and 17.42, respectively.

IV. FINITE ELEMENT MODEL VERIFICATION

To demonstrate the impact of the approximated fan-shaped PM fraction on the accuracy of the 2-D SAM, four cases are defined in this section. With one fan-shaped region in the first case, two in the second, three in the third, and four in the fourth, the rectangular PM is approximated by these cases, respectively. The FE model is established in the FE software JMAG, and the main parameters of the studied motor are listed in Table IV. Fig. 9(a) and (b) shows the MFD under no-load and load conditions, respectively. Matrix (26) is solved in MATLAB to obtain the MFD and EPs. In each case, the MFD and electromagnetic parameters obtained by the analytical model are compared with the FE model.

A. Comparison of Magnetic Field Distribution

In Figs. 10 and 11, the comparison of the air gap flux density components between the FE model and the proposed nonlinear SAM is given. The waveforms and harmonic spectrums show that the analytical results are closer to the FE model as the number of fan-shaped approximation PM pieces increases. When the number of approximated PM pieces is four, the above two calculation methods are very consistent.

Additionally, as shown in Fig. 12, the air gap flux density components under load conditions are compared when the phase current is 10 A. It is apparent that when the number of approximated blocks of PMs increases, the computation accuracy improves as well.

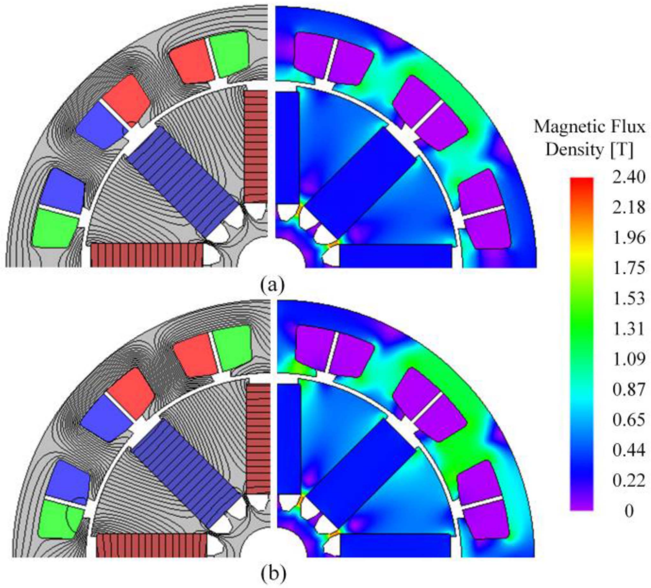

Fig. 9. FE models. (a) No-load condition. (b) On-load condition.

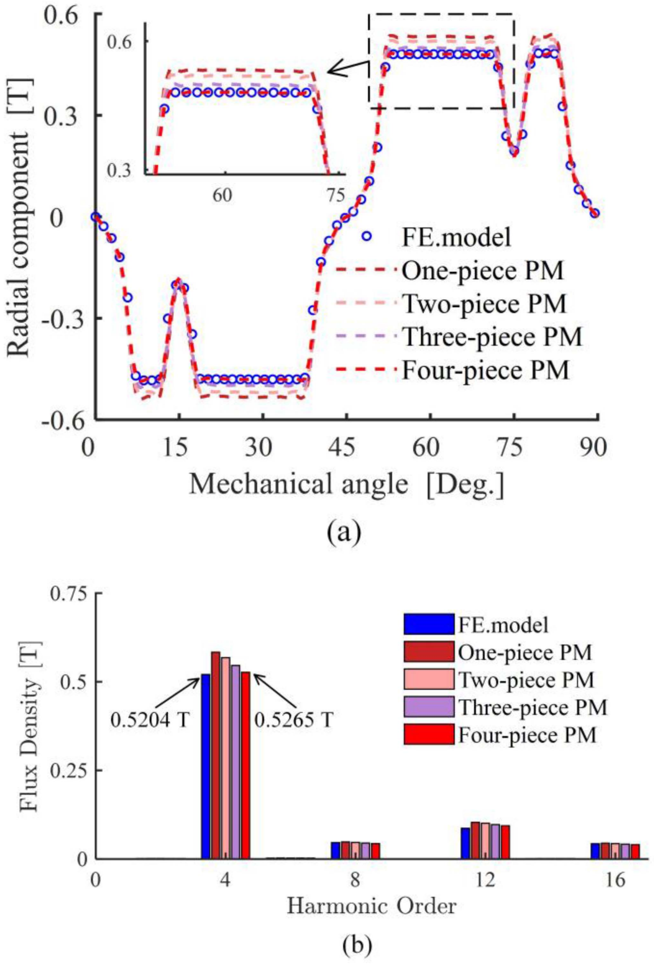

Fig. 10. Comparison of radial components of no-load flux density in the air gap. (a) Waveforms. (b) Harmonic spectrum.

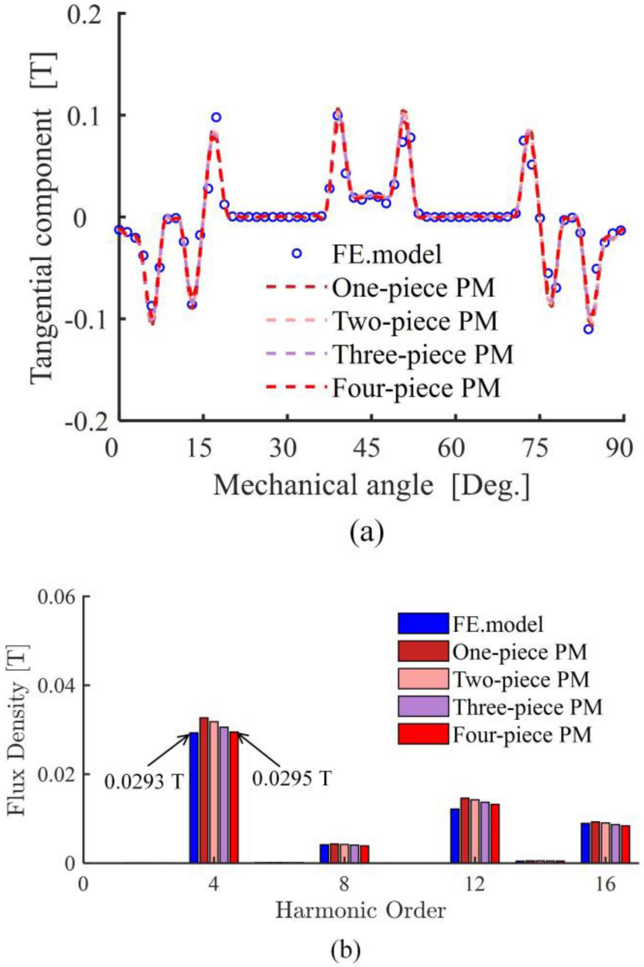

(a)

(b)

Fig. 11. Comparison of tangential components of no-load flux density in the air gap. (a) Waveforms. (b) Harmonic spectrum.

B. Comparison of Electromagnetic Performances

Figs. 13 and 14 compare the no-load EPs, namely cogging torque and back EMF. Even though there are calculation errors in the first to third cases, these errors get smaller as there are more approximations of PM regions. In the fourth case, the EPs predicted by the SAM are basically consistent with the FE model calculation results.

In particular, the self- and mutual inductances of phase A are calculated. Fig. 15 shows the comparison between the analytical model (four-piece PM) and the FE model for the variation of self- and mutual inductances with rotor position. Both results obtained from the SAM are in very good agreement with those obtained by the FE model. The maximum and minimal values of the self-inductance are, respectively, $L_{a,\max} = 0.1813$ mH and $L_{a,\min} = 0.1536$ mH for the SAM and $L_{a,\max} = 0.1799$ mH and $L_{a,\min} = 0.1545$ mH for the FE model.

Furthermore, the electromagnetic torque for each case is evaluated at rated current $I = 10$ A, as illustrated in Fig. 16. It is clear that they have the same variation trends. To visual interpretation of the calculation accuracy, Table V lists the

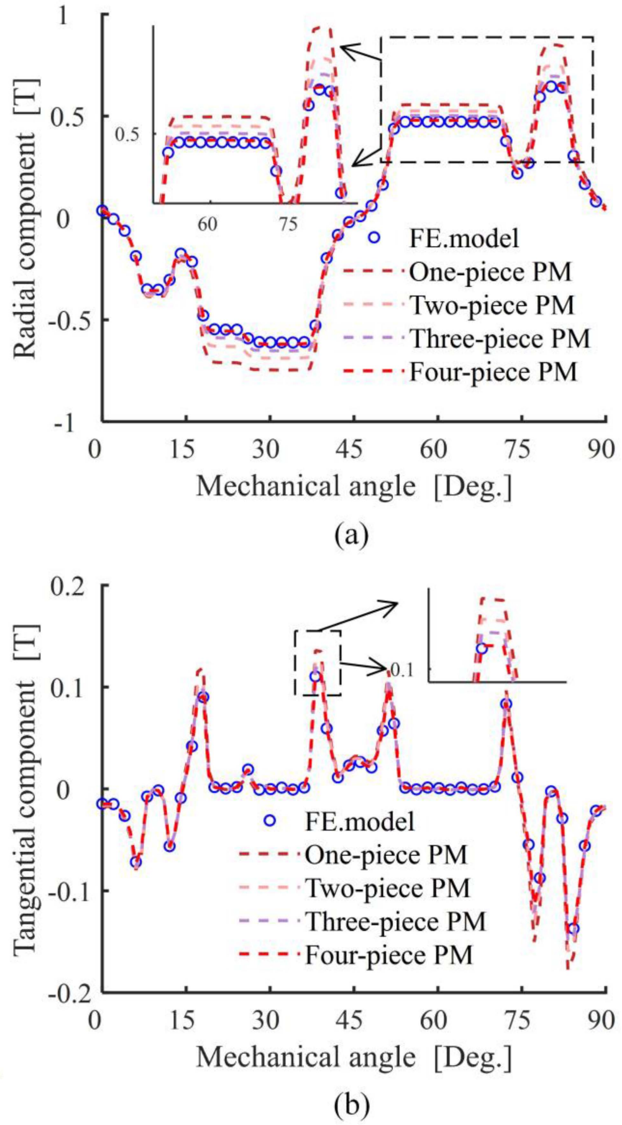

(a)

(b)

Fig. 12. Comparison of on-load air gap flux density components. (a) Radial component. (b) Tangential component.

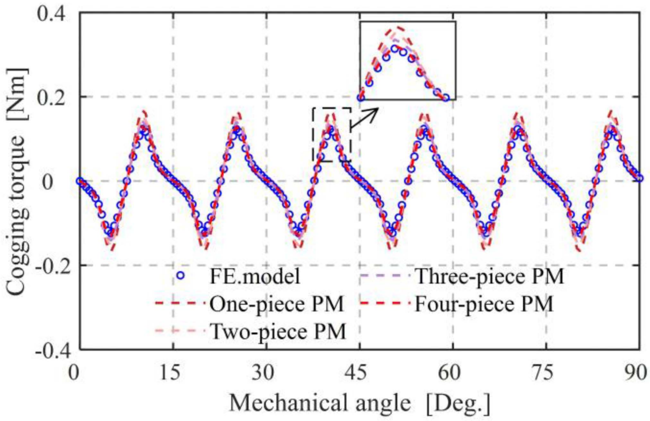

Fig. 13. Comparison of cogging torque.

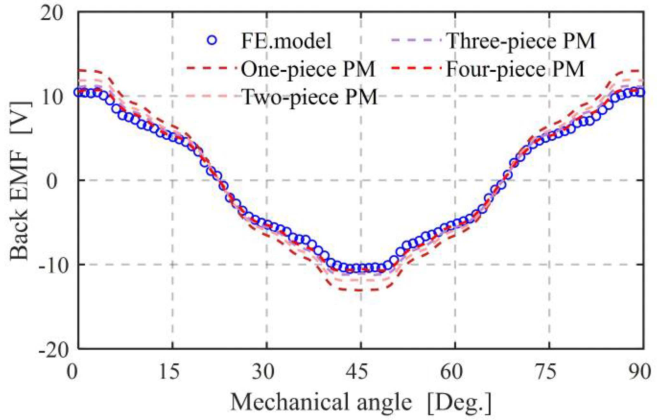

Fig. 14. Comparison of back EMFs at 3000 r/min.

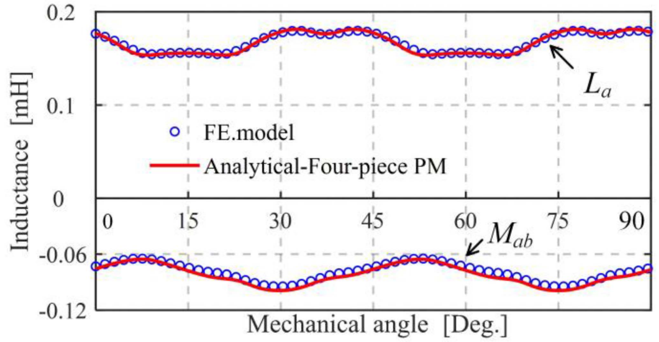

Fig. 15. Comparison of self/mutual inductance (L_a and M_{ab}).

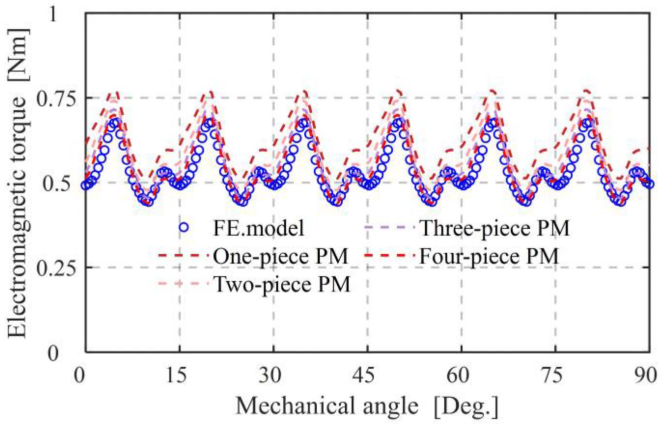

Fig. 16. Comparison of electromagnetic torque.

TABLE V
COMPARISON OF ELECTROMAGNETIC TORQUE

Items	FE model	1-piece	2-piece	3-piece	4-piece
Average T_{em}	0.536Nm	0.628Nm	0.590Nm	0.565Nm	0.548Nm
Relative error	-	17.16%	10.07%	5.41%	2.23%

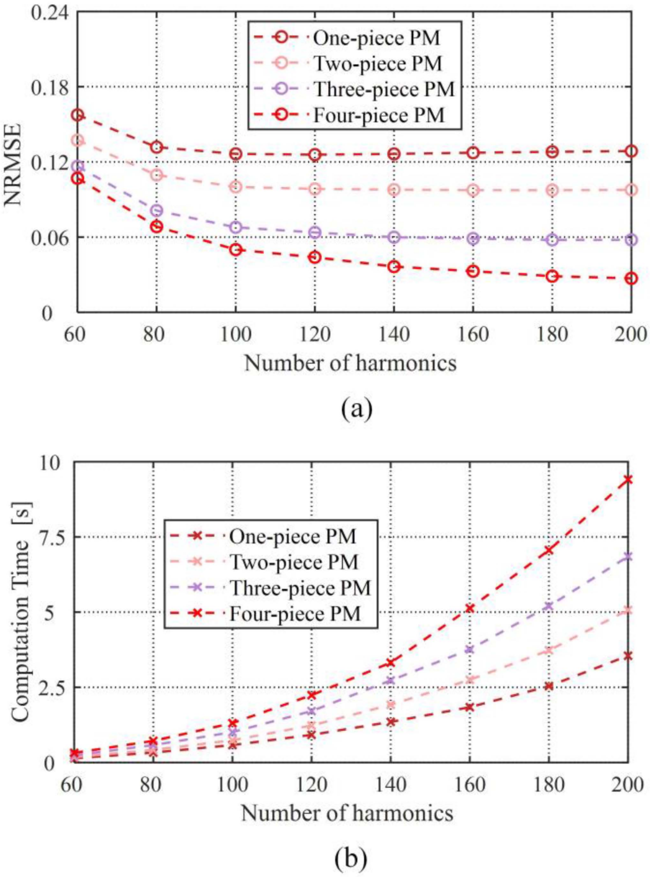

(a)

(b)

Fig. 17. Influence of the number of harmonics on (a) NRMSE of the radial magnetic flux density in the air-gap and (b) computation time.

average torque and relative error of the above calculation cases. As the number of approximate PMs increases, the calculation error of average electromagnetic torque decreases gradually. In particular, when the fan-shaped PMs are four, the relative error of the average electromagnetic torque is only 2.23%, and an acceptable agreement has been achieved.

C. Computation Time

The number of calculation regions affects the computation time of the analytical model proposed in this article, but the selection of harmonic numbers also has a significant impact. The normalized root mean square of error (NRMSE) of the no-load magnetic density in each case is calculated as follows to visually illustrate the calculation accuracy

$$\text{NRMSE} = \sqrt{\frac{\sum_i^{N_{pc}} \left[B_{Ana}(i) - B_{FEM}(i)\right]^2}{\sum_i^{N_{pc}} B_{FEM}(i)^2}} \tag{37}$$

where $B_{Ana}(i)$ and $B_{FEM}(i)$ are values of the ith estimation of magnetic flux density, respectively, by SAM and FE model; N_{pc} is the number of test data.

In Fig. 17, the NRMSE of the radial magnetic flux density in the air-gap and calculation time of the SAM is shown as a function of the number of harmonics. All calculations are

TABLE VI
COMPUTATION TIME COMPARISONS OF DIFFERENT CASES

	1-piece	2-piece	3-piece	4-piece
Linear SAM/s	1.16	1.60	2.14	2.86
Nonlinear SAM/s	8.59	14.31	18.77	24.52
Nonlinear FE model/s	30.58			

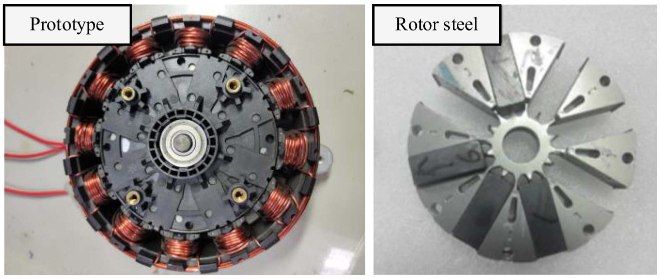

(a) (b)

Fig. 18. Structure of the prototype. (a) Prototype. (b) Rotor steel.

performed at the center of air-gap for $N_{pc} = 500$ different points along the circumference. It can be seen from Fig. 17(a) that the NRMSE of each case already starts to converge around N = 120. To make a compromise between calculating efficiency and accuracy, the maximum harmonic order N for computation in this article is set to 130. Both analytical models and FE models are run on a PC with Intel (R) Core (TM) i7-7700k CPU @ 4.20 GHz and 16 GB main memory under the WIN10 operating environment. The computation time of SAM (linear and nonlinear) and nonlinear FE model for single-step MFD is listed in Table VI. It can be seen that as the number of approximate PMs increases, the computational time of the SAM also increases. This is because for each additional calculation region, 2 × (2 × N + 1) unknown coefficients are added. In addition, the computational time of the nonlinear SAM is several times that of the linear SAM. This is because the nonlinear SAM uses the iterative algorithm proposed in Section III to consider the nonlinearity of ferromagnetic materials, which is equivalent to several repetitions of the linear SAM. In the fourth case, a proper compromise between calculation time and accuracy is achieved. The calculation time of the nonlinear SAM is 80% of the nonlinear FE model, while the linear SAM is only 10%. The computational time of the nonlinear SAM depends on the convergence error Δ and the maximum number of iterations $M_{\max}$. Thanks to the efficient computational efficiency of the linear SAM model, it has important application prospects in the design and optimization of PM motors.

V. EXPERIMENTAL VERIFICATION

In this section, the phase inductance, back EMF, and output torque experiments of a 12-slot/8-pole cubic spoke-type PM machine are carried out to verify the effectiveness of the nonlinear SAM proposed in this article. The structure of the prototype is shown in Fig. 18.

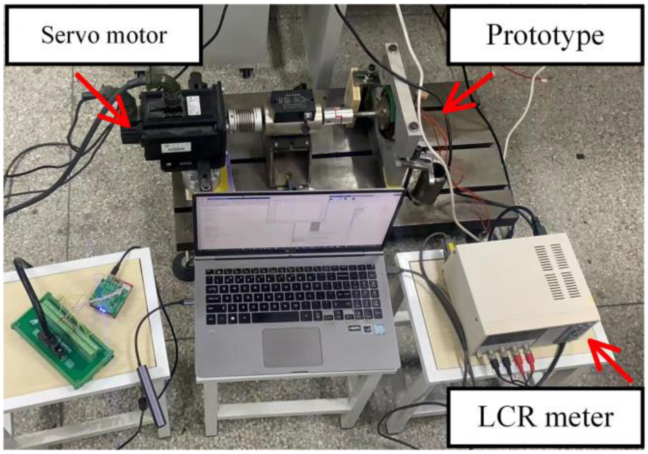

Fig. 19. Inductance measurement setup.

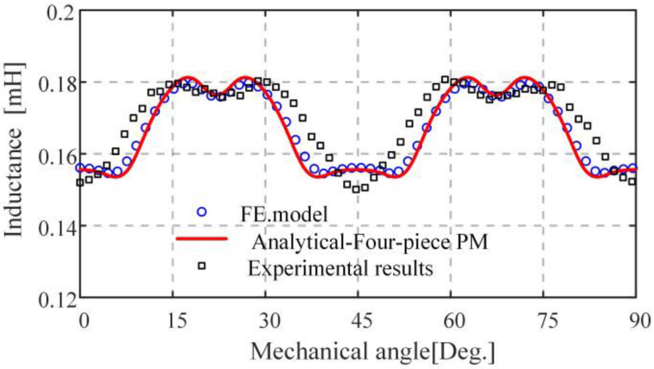

Fig. 20. Comparison of phase inductance.

To verify the correctness of the proposed method, the phase inductance of different rotor positions is measured by LCR meter, and the measurement setup is shown in Fig. 19. Fig. 20 shows the comparison between the measured and calculated phase inductances at different rotor positions. It can be found that the experimental waveform is slightly different from the analytical and FE results because the rotor structure is simplified in the analytical model and the FE model [i.e., the effect of the weight reduction hole is ignored, as can be seen in Fig. 18(b)]. The maximum values of the phase inductance $L_{\max}$ of the experiment and SAM are 0.1817 mH and 0.1813 mH, respectively; the minimum values of experimental and SAM are 0.1498 mH and 0.1536 mH, respectively, and the relative error is 2.54%.

To test the no-load back EMF of the prototype, the prototype is driven by a servo motor. Fig. 21 illustrates the experimental setup and devices. The servo motor is set to speed control mode and runs at 1200 r/min. The experimental results of back EMFs are shown in Fig. 22. As can be seen, the experimental results and the four-piece approximation model match well. The experimental result has an RMS value of 2.96 V, while the proposed nonlinear SAM computes a value of 3.04 V, and the relative error is only 2.7%. The predicted waveform shape by nonlinear SAM and the experimental waveform, however, differ slightly. It is primarily due to the analytical model neglecting the rotor chamfer's influence.

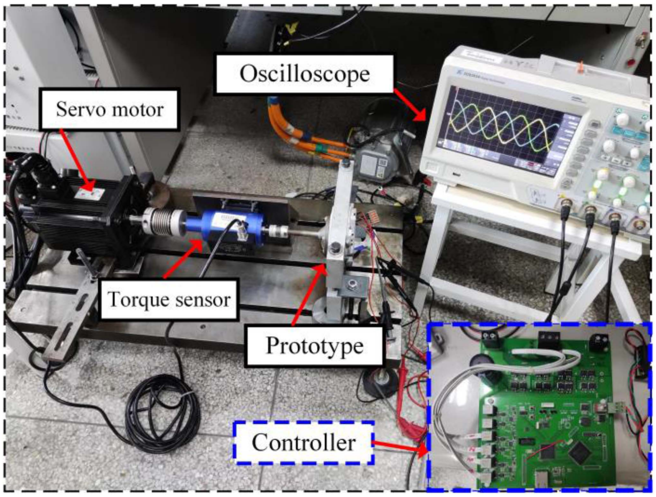

Fig. 21. Experimental setup.

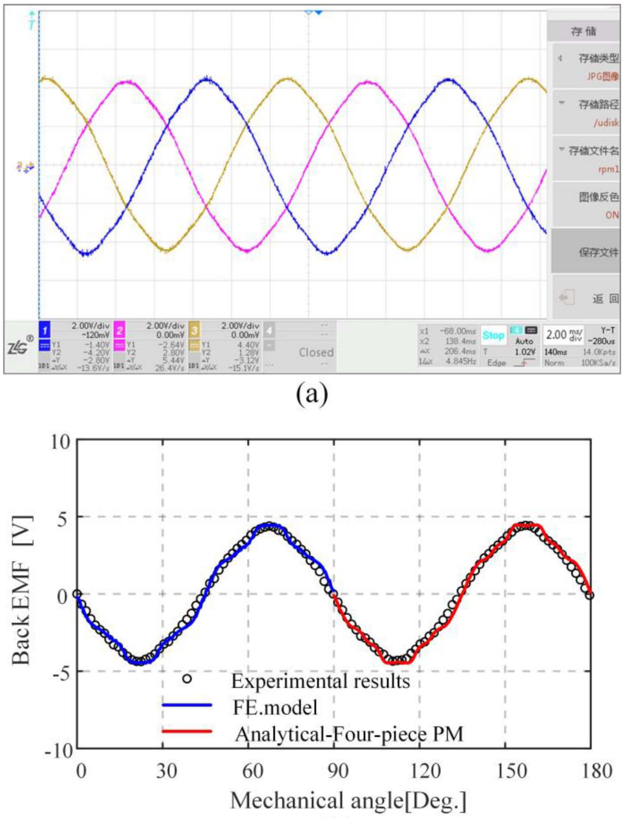

(a)

(b)

Fig. 22. Experimental result of back EMFs. (a) Experimental results. (b) Comparison of back EMF of phase A.

The output torque of the prototype is then tested. The prototype is controlled by position sensorless field-oriented control (FOC), and the servo motor runs as a generator. The output torque is measured with a high-precision torque sensor. The output torque was tested at 1500 r/min, and the amplitude of the phase current varied from 5 to 20 A. The current waveform at a phase current amplitude of 20 A is presented in Fig. 23(a), while the current in the analytical model and the FE model is a completely sinusoidal current, which also causes errors in the output torque results. Fig. 23(b) shows the current versus torque curve. Table VII provides the specific information for the current and output torque at 1500 r/min. It can be seen that when the current is lower than 12 A, the relative error is less than 5%; on the other hand, as the current increases, the degree of magnetic saturation deepens. The relative error rises to 6.7% at 20 A (200% of the rated current), which is still within an acceptable range.

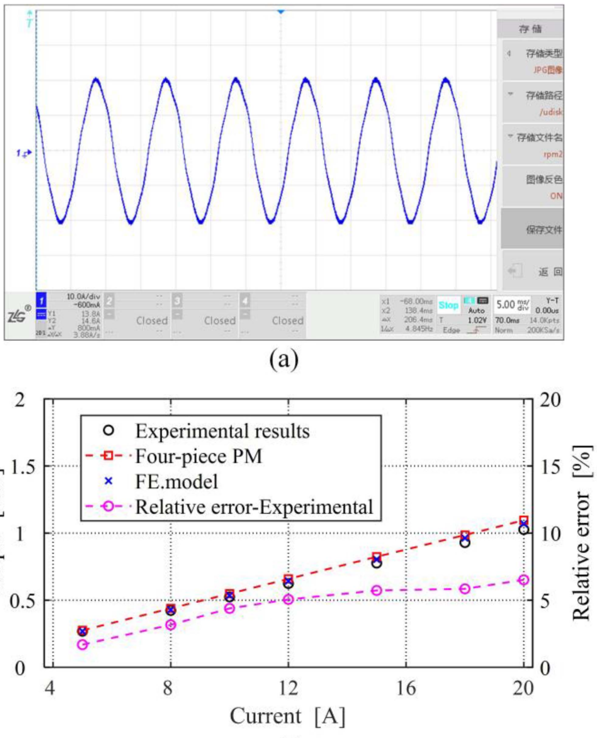

(a)

(b)

Fig. 23. Output torque. (a) 20 A phase current waveform. (b) Current versus torque curve.

TABLE VII
CURRENT AND TORQUE DATA AT 1500 R/MIN

Current /A	5	8	10	12	15	18	20
Test /Nm	0.269	0.424	0.525	0.625	0.777	0.93	1.027
FE model /Nm	0.269	0.429	0.536	0.643	0.804	0.963	1.07
SAM /Nm	0.274	0.437	0.548	0.657	0.822	0.984	1.094

In addition, the capability in the transient of the proposed method is also given. The dynamic characteristic of the studied motor is tested and compared with the analytical and FE model results, the torque–speed characteristic is shown in Fig. 24. The motor runs under double overload condition at 100–600 r/min; then runs at the rated load condition. When the motor speed exceeds 1600 r/min, the line voltage of the motor is close to the bus voltage of the power supply, the motor runs at 1600–2400 r/min in the state of flux-weakening. It can be seen that the proposed method can obtain the dynamic characteristics of the motor in the full speed range, and the analytical results are in good agreement with the FE model results and experimental results.

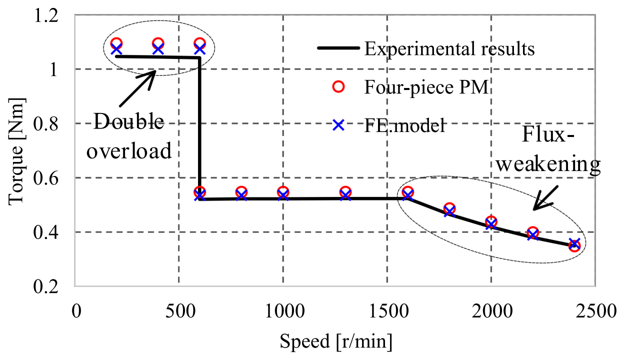

Fig. 24. Torque–speed characteristic of the studied motor.

VI. CONCLUSION

This article proposed an improved 2-D analytical modeling approach for cubic spoke-type PM machines based on dividing the inconsistent rectangular region into multiple consistent fan-shaped subregions in polar coordinates. To find the appropriate combination of fan-shaped PM fractions and the number of harmonics under the constraints of computation efficiency and accuracy, four cases were investigated. The four fan-shaped PM segments are an appropriate tradeoff between time and accuracy, and the nonlinear SAM can save 20% of the calculation time compared to the nonlinear FE model, while the linear SAM is faster. Furthermore, the approach presented in this research can be extended to V-type or U-type interior PM motors to provide an efficient computing tool to speed up their design and optimization.

REFERENCES

[1] M.-J. Jeong, K.-B. Lee, H.-J. Pyo, D.-W. Nam, and W.-H. Kim, “A study on the shape of the rotor to improve the performance of the spoke-type permanent magnet synchronous motor,” *Energies*, vol. 14, Jan. 2021, Art. no. 13, doi: 10.3390/en14133758.

[2] S. G. Lee, J. Bae, and W.-H. Kim, “Study on the axial leakage magnetic flux in a spoke type permanent magnet synchronous motor,” *IEEE Trans. Ind. Appl.*, vol. 55, no. 6, pp. 5881–5887, Nov./Dec. 2019, doi: 10.1109/TIA.2019.2939743.

[3] W. Liu and T. A. Lipo, “Analysis of consequent pole spoke type vernier permanent magnet machine with alternating flux barrier design,” *IEEE Trans. Ind. Appl.*, vol. 54, no. 6, pp. 5918–5929, Nov./Dec. 2018, doi: 10.1109/TIA.2018.2856579.

[4] Q. Chen, G. Xu, F. Zhai, and G. Liu, “A novel spoke-type PM motor with auxiliary salient poles for low torque pulsation,” *IEEE Trans. Ind. Electron.*, vol. 67, no. 6, pp. 4762–4773, Jun. 2020, doi: 10.1109/TIE.2019.2924864.

[5] A. Fatemi, D. M. Ionel, M. Popescu, Y. C. Chong, and N. A. O. Demerdash, “Design optimization of a high torque density spoke-type PM motor for a Formula E race drive cycle,” *IEEE Trans. Ind. Appl.*, vol. 54, no. 5, pp. 4343–4354, Sep./Oct. 2018, doi: 10.1109/TIA.2018.2844804.

[6] M. Kimiabeigi et al., “High-performance low-cost electric motor for electric vehicles using ferrite magnets,” *IEEE Trans. Ind. Electron.*, vol. 63, no. 1, pp. 113–122, Jan. 2016, doi: 10.1109/TIE.2015.2472517.

[7] X. Liu, H. Chen, J. Zhao, and A. Belahcen, “Research on the performances and parameters of interior PMSM used for electric vehicles,” *IEEE Trans. Ind. Electron.*, vol. 63, no. 6, pp. 3533–3545, Jun. 2016, doi: 10.1109/TIE.2016.2524415.

[8] Y. Zhou, Y. Chen, and J.-X. Shen, “Analysis and improvement of a hybrid permanent-magnet memory motor,” *IEEE Trans. Energy Convers.*, vol. 31, no. 3, pp. 915–923, Sep. 2016, doi: 10.1109/TEC.2015.2507262.

[9] D.-K. Lim, K.-P. Yi, S.-Y. Jung, H.-K. Jung, and J.-S. Ro, “Optimal design of an interior permanent magnet synchronous motor by using a new surrogate-assisted multi-objective optimization,” *IEEE Trans. Magn.*, vol. 51, no. 11, Nov. 2015, Art. no. 8207504, doi: 10.1109/TMAG.2015.2449872.

[10] B. Guo, Y. Huang, F. Peng, and J. Dong, “A new hybrid method for magnetic field calculation in IPMSM accounting for any rotor configuration,” *IEEE Trans. Ind. Electron.*, vol. 66, no. 7, pp. 5015–5024, Jul. 2019, doi: 10.1109/TIE.2018.2868252.

[11] T. A. Driscoll and L. N. Trefethen, *Schwarz-Christoffel Mapping*. Cambridge, U.K., MA, USA: Cambridge Univ. Press, 2002.

[12] K. Boughrara, T. Lubin, and R. Ibtiouen, “General subdomain model for predicting magnetic field in internal and external rotor multiphase flux-switching machines topologies,” *IEEE Trans. Magn.*, vol. 49, no. 10, pp. 5310–5325, Oct. 2013, doi: 10.1109/TMAG.2013.2260827.

[13] K. Boughrara, R. Ibtiouen, and T. Lubin, “Analytical prediction of magnetic field in parallel double excitation and spoke-type permanent-magnet machines accounting for tooth-tips and shape of polar pieces,” *IEEE Trans. Magn.*, vol. 48, no. 7, pp. 2121–2137, Jul. 2012, doi: 10.1109/TMAG.2012.2186587.

[14] M. Hajdinjak and D. Miljavec, “Analytical calculation of the magnetic field distribution in slotless brushless machines with U-shaped interior permanent magnets,” *IEEE Trans. Ind. Electron.*, vol. 67, no. 8, pp. 6721–6731, Aug. 2020, doi: 10.1109/TIE.2019.2939967.

[15] B. Guo et al., “Nonlinear semianalytical model for axial flux permanent-magnet machine,” *IEEE Trans. Ind. Electron.*, vol. 69, no. 10, pp. 9804–9816, 2022, doi: 10.1109/TIE.2022.3159952.

[16] F. Dubas and K. Boughrara, “New scientific contribution on the 2-D subdomain technique in cartesian coordinates: Taking into account of iron parts,” *Math. Comput. Appl.*, vol. 22, Mar. 2017, Art. no. 1, doi: 10.3390/mca22010017.

[17] F. Dubas and K. Boughrara, “New scientific contribution on the 2-D subdomain technique in polar coordinates: Taking into account of iron parts,” *Math. Comput. Appl.*, vol. 22, Dec. 2017, Art. no. 4, doi: 10.3390/mca22040042.

[18] L. Roubache, K. Boughrara, F. Dubas, and R. Ibtiouen, “Elementary subdomain technique for magnetic field calculation in rotating electrical machines with local saturation effect,” *Int. J. Comput Math. Elect. Electron. Eng.*, vol. 38, no. 1, pp. 24–45, Jan. 2018, doi: 10.1108/COMPEL-11-2017-0481.

[19] R. L. J. Sprangers, J. J. H. Paulides, B. L. J. Gysen, J. Waarma, and E. A. Lomonova, “Semianalytical framework for synchronous reluctance motor analysis including finite soft-magnetic material permeability,” *IEEE Trans. Magn.*, vol. 51, no. 11, Nov. 2015, Art. no. 8110504, doi: 10.1109/TMAG.2015.2442419.

[20] R. L. J. Sprangers, J. J. H. Paulides, B. L. J. Gysen, and E. A. Lomonova, “Magnetic saturation in semi-analytical harmonic modeling for electric machine analysis,” *IEEE Trans. Magn.*, vol. 52, no. 2, Feb. 2016, Art. no. 8100410, doi: 10.1109/TMAG.2015.2480708.

[21] Z. Djelloul-Khedda, K. Boughrara, F. Dubas, and R. Ibtiouen, “Nonlinear analytical prediction of magnetic field and electromagnetic performances in switched reluctance machines,” *IEEE Trans. Magn.*, vol. 53, no. 7, Jul. 2017, Art. no. 8107311, doi: 10.1109/TMAG.2017.2679686.

[22] Z. Djelloul-Khedda, K. Boughrara, F. Dubas, A. Kechroud, and A. Tikellaline, “Analytical prediction of iron-core losses in flux-modulated permanent-magnet synchronous machines,” *IEEE Trans. Magn.*, vol. 55, no. 1, 2019, Art. no. 6300112, doi: 10.1109/TMAG.2018.2877164.

[23] H. Zhao, C. Liu, Z. Song, and J. Yu, “A fast optimization scheme of coaxial magnetic gears based on exact analytical model considering magnetic saturation,” *IEEE Trans. Ind. Appl.*, vol. 57, no. 1, pp. 437–447, Jan./Feb. 2021, doi: 10.1109/TIA.2020.3040142.

[24] Z. Djelloul-Khedda, K. Boughrara, F. Dubas, A. Kechroud, and B. Souleyman, “Semi-analytical magnetic field predicting in many structures of permanent-magnet synchronous machines considering the iron permeability,” *IEEE Trans. Magn.*, vol. 54, no. 7, Jul. 2018, Art. no. 8103921, doi: 10.1109/TMAG.2018.2824278.

[25] B. Ladghem Chikouche and R. Ibtiouen, “Analytical approach for spoke-type permanent magnet machine including finite permeability of iron core,” *Int. J. Comput. Math. Elect. Electron. Eng.*, vol. 39, no. 2, pp. 333–352, Jan. 2020, doi: 10.1108/COMPEL-04-2019-0143.

[26] K. J. Meessen, B. L. J. Gysen, J. J. H. Paulides, and E. A. Lomonova, “Halbach permanent magnet shape selection for slotless tubular actuators,” *IEEE Trans. Magn.*, vol. 44, no. 11, pp. 4305–4308, Nov. 2008, doi: 10.1109/TMAG.2008.2001536.

[27] M. Pourahmadi-Nakhli, A. Rahideh, and M. Mardaneh, "Analytical 2-D model of slotted brushless machines with cubic spoke-type permanent magnets," *IEEE Trans. Energy Convers.*, vol. 33, no. 1, pp. 373–382, Mar. 2018, doi: 10.1109/TEC.2017.2726537.

[28] P. Liang, F. Chai, Y. Li, and Y. Pei, "Analytical prediction of magnetic field distribution in spoke-type permanent-magnet synchronous machines accounting for bridge saturation and magnet shape," *IEEE Trans. Ind. Electron.*, vol. 64, no. 5, pp. 3479–3488, May 2017, doi: 10.1109/TIE.2016.2644598.

[29] P. Liang, F. Chai, Y. Yu, and L. Chen, "Analytical model of a spoke-type permanent magnet synchronous In-wheel motor with trapezoid magnet accounting for tooth saturation," *IEEE Trans. Ind. Electron.*, vol. 66, no. 2, pp. 1162–1171, Feb. 2019, doi: 10.1109/TIE.2018.2831194.

[30] P. Liang, F. Chai, L. Chen, and Y. Wang, "Analytical prediction of No-load stator iron losses in spoke-type permanent-magnet synchronous machines," *IEEE Trans. Energy Convers.*, vol. 33, no. 1, pp. 252–259, Mar. 2018, doi: 10.1109/TEC.2017.2737701.

[31] H. C. Lovatt and P. A. Watterson, "Energy stored in permanent magnets," *IEEE Trans. Magn.*, vol. 35, no. 1, pp. 505–507, Jan. 1999, doi: 10.1109/20.737473.

[32] A. Hemeida and P. Sergeant, "Analytical modeling of surface PMSM using a combined solution of Maxwell's equations and magnetic equivalent circuit," *IEEE Trans. Magn.*, vol. 50, no. 12, Dec. 2014, Art. no. 7027913, doi: 10.1109/TMAG.2014.2330801.

Yunlu Du (Student Member, IEEE) received the B.S. degree in electrical engineering from Anhui University, Hefei, China, in 2020. He is currently working toward the Ph.D. degree in electrical engineering with the School of Electrical Engineering, Southeast University, Nanjing, China.

His main research interests include electromagnetic field computation and permanent magnet motor design.

Yunkai Huang received the M.Sc. and Ph.D. degrees in electrical engineering from Southeast University, Nanjing, China, in 2001 and 2007, respectively.

He is currently a Professor with the School of Electrical Engineering, Southeast University and teaching "Electrical Machinery" and "Digital Signal Processing." His research interests include design and control of PM machine and high speed machine, applications in domestic appliances, electric vehicles, railway traction, all electric ships, and wind power generation systems.

Baocheng Guo (Member, IEEE) received the B.E. degree in electrical engineering from China University of Petroleum, Qingdao, China, in 2009, the M.E. degree in electrical engineering from Harbin University of Science and Technology, Harbin, China, in 2014, and the Ph.D. degree in electrical engineering from Southeast university, Nanjing, China in 2017.

He is currently an Associate Professor with Nanjing Normal University, Nanjing, since 2022. Before joining NNU, he was a Postdoctoral Researcher with Southeast university. His main interests are the electromagnetic field computation, and development of fast multiphysics models of electrical machines.

Zakarya Djelloul-Khedda was born in Chlef, Algeria, in 1988. He received the B.Sc. degree in electronics communication system and M.Sc. degree in industrial information technology from Hassiba Benbouali University of Chlef, Chlef, Algeria, in 2009 and 2011, respectively, and the Ph.D. degree in electrical engineering from Djilali Bounaama University of Khemis Miliana, Khemis Miliana, Algeria, in 2019. He is currently with SONELGAZ-Distribution Company of SONELGAZ Group, Chlef, Algeria, which is an Algerian National Group of companies responsible for the production, transmission, and distribution of electricity and natural gas. His current research interests include design, modeling, optimization, and control of electrical machines.

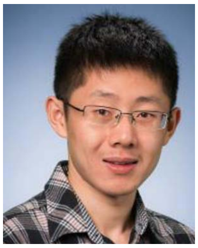

Fei Peng (Member, IEEE) received the B.S. and M.S. degrees in electrical engineering from Southeast University, Nanjing, China, in 2010 and 2012, respectively. He received the Ph.D. degree in electrical and computer engineering from McMaster University, Hamilton, ON, Canada, in 2016.

After that he was a Postdoctoral Fellow with the McMaster Institute for Automotive Research and Technology, McMaster University. His research interests include optimal design and control of power converters, modeling, and digital control of motor drives.

Yu Yao (Student Member, IEEE) received the B.S. and Ph.D. degrees in electrical engineering from Southeast University, Nanjing, China, in 2016 and 2022, respectively. After that, he joined the School of Electrical Engineering at Southeast University, as an Assistant Professor.

His main research interests include the design of the power inverter, the current regulator design, the position sensorless drive for the high-speed PMSM and the drive system with *LCL* output filter.

Jianning Dong (Member, IEEE) received the B.S. and Ph.D. degrees in electrical engineering from Southeast University, Nanjing, China, in 2010 and 2015, respectively.

Since 2016, he has been an Assistant Professor with the DC System, Energy Conversion and Storage (DCE&S) Group, Delft University of Technology (TU Delft), Delft, The Netherlands. Before joining TU Delft, he was a Postdoctoral Researcher with McMaster Automotive Resource Centre, McMaster University, Hamilton, ON, Canada. His research interests include electromechanical energy conversion and contactless power transfer.